

Investigation of $^{9,10}\text{Be}$ weakly bound nuclei elastically scattered from ^{208}Pb

Sh. Hamada

Faculty of Science, Tanta University, Tanta, Egypt.

Awad A. Ibraheem

*Physics Department, King Khalid University, Abha, Saudi Arabia,
Physics Department, Al-Azhar University, Assiut Branch, Assiut 71524, Egypt.*

Received 1 December 2021; accepted 8 January 2022

Experimental angular distributions for the weakly bound $^{9,10}\text{Be}$ nuclei elastically scattered from ^{208}Pb target at various energies are investigated using phenomenological and microscopic potentials. The considered data in this study are: $^9\text{Be}+^{208}\text{Pb}$ in the energy range of 37.0 – 75.0 MeV and $^{10}\text{Be}+^{208}\text{Pb}$ in the energy range of 38.4 – 43.9 MeV. The performed analysis reflects the nature and peculiarities of the considered projectiles. For the $^9\text{Be}+^{208}\text{Pb}$ nuclear system, the data showed a typical Fresnel diffraction scattering pattern and the Coulomb rainbow phenomenon is well presented due to the interference between partial waves refracted by the Coulomb and nuclear potentials. The $^7\text{Li}+d$ and $^9\text{Be}+n$ cluster structures of ^9Be and ^{10}Be , respectively are studied. The extracted renormalization factors for the real part of potential constructed on the basis of double folding as well as cluster folding could reflect the nature of the loosely bound projectiles.

Keywords: Elastic scattering; phenomenological potential; Cluster folding; Coupled channels; Breakup potential.

DOI: <https://doi.org/10.31349/RevMexFis.68.041202>

1. Introduction

Recently, with the increasing possibility and availability of accelerating different radioactive beams, many nuclear processes induced by different weakly bound nuclei have become a hot topic of research. Due to the weak binding for these nuclei, the coupling effect to break-up channels is expected to increase. The break-up effect observed in ^6Li and ^7Li projectiles for example, is found to play a key role in exhibiting some abnormalities such as the necessity to reduce the strength of double folding (DF) potential by about 30–50 % in order to reproduce the experimental data. The same situation was also reported while using cluster folding potential in reproducing the experimental data for nuclear systems induced by $^{6,7}\text{Li}$ ion beams [1–8]. Other interesting weakly bound nuclei are the $^{9,10}\text{Be}$ isotopes which are subjected to a detailed analysis in current work in order to probe their interaction mechanism with the heavy ^{208}Pb target [9–12].

However, ^9Be is another anomalous projectile that requires significantly less renormalization than unity. In the tail region of $^{6,7}\text{Li}$, the imaginary potential is diffuse and stronger than the real potential. ^9Be , like $^{6,7}\text{Li}$, is loosely bound, breaking up into $n+2\alpha$ with only 1.57 MeV. The odd neutron in ^9Be is only bound by 1.367 MeV, and Satchler has shown that the potential depth near the strong absorption radius is strongly influenced by the neutron density treatment [13–16].

Elastic scattering processes between two colliding nuclei still remain an important topic in nuclear physics studies. The angular distributions of elastic scattering cross sections can exhibit different features depending on the structure of the two colliding nuclei and on the projectile's energy. For stable projectiles, and at energies close to the Coulomb bar-

rier, Fresnel oscillatory diffraction pattern may appear when the angular distributions are plotted as a ratio to Rutherford cross sections. This Fresnel peak, usually called Coulomb rainbow, is due to the interference between partial waves refracted by the Coulomb and short-range nuclear potentials. For light projectiles, the Coulomb force becomes smaller and the diffractive pattern changes from Fresnel to Fraunhofer oscillations at higher energies. The data from our previous study [17] of the interaction mechanism of weakly bound $^{9,10,11}\text{Be}$ scattered from ^{64}Zn were analyzed using both the conventional optical model (OM) and the double folding optical model (DFOM). The elastic scattering angular distributions for $^{9,10}\text{Be}$ isotopes are well reproduced both by the phenomenological OM as well as the DFOM with the suitable optimized parameter sets, while for the ^{11}Be isotope, the strong reduction of the cross section around the nuclear-Coulomb interference angles can not be reproduced by the DFOM. The reasonable fit to the data is only achieved by adding a very long-range absorption term in the imaginary part. The differences in the extracted renormalization factor (N_r) values for the different considered nuclear systems induced by Be isotopes could reflect the difference of weak binding nature among the three studied Be isotopes.

In this paper, both pure phenomenological and semi-microscopic potentials are used to investigate the interaction mechanism for the weakly bound $^{9,10}\text{Be}$ nuclei scattered from ^{208}Pb target at various available energies. In connection with this aim, the following data are analyzed: $^9\text{Be}+^{208}\text{Pb}$ in the energy range 37.0 – 75.0 MeV [9,11] and $^{10}\text{Be}+^{208}\text{Pb}$ in the energy range 38.4–43.9 MeV [10, 12].

The paper is organized as follows. Section 2 discusses the nuclear potentials that are used in the data analysis, while

Sec. 3 discusses the results and discussion. The summary is provided in Sec. 4.

2. Theoretical methods

As a first step for probing the interaction mechanism for the considered nuclear systems, OM of the nucleus is applied. The implemented phenomenological OM potential has the following form:

$$U(r) = V_C - V_0 \left(1 + \exp \left[\frac{r - R_V}{a_V} \right] \right)^{-1} - iW_0 \left(1 + \exp \left[\frac{r - R_W}{a_W} \right] \right)^{-1}. \quad (1)$$

The $V_C(r)$ is the Coulomb potential due to a uniform sphere with a charge equal to that of the target nucleus and radius $r_C A_t^{1/3}$. The nuclear potential is consisting from two parts: real volume (which simulate the scattering) and imaginary volume (simulate the reduction in flux due to absorption), both has the phenomenological Woods-Saxon (WS) shape.

In the semi-microscopic analysis, the real part of the potential was constructed based on the DF procedures as,

$$V_{DF}(r) = \iint \rho_p(r_1) \rho_t(r_2) v_{NN}(S) d^3r_1 d^3r_2, \quad (2)$$

where $\rho_p(r_1)$, $\rho_t(r_2)$ are the matter densities of the projectile and the target respectively and $v_{NN}(S)$ is the effective NN interaction between two nucleons where $S = \vec{R} - \vec{r}_1 + \vec{r}_2$. For NN effective interactions, the widely held choosing has been based on the M3Y interactions which were designed to reproduce the G-matrix elements of Paris [18-20] NN interactions. The density distribution of ${}^9\text{Be}$ is deduced using the Argonne v18 two-nucleon and Urbana X three-nucleon potentials (AV18+UX) in a realistic Variational Monte Carlo (VMC) wave function [21]. For the density distributions of ${}^{10}\text{Be}$ and ${}^{208}\text{Pb}$, the following fermi form is assumed [22,23].

$$\rho(r) = \frac{\rho_0}{1 + \exp(r - R)/a}. \quad (3)$$

For ${}^{10}\text{Be}$ (${}^{208}\text{Pb}$), $R = 2.0$ (6.80) fm , $a = 0.511$ (0.515) fm and root-mean-square (rms) matter radius of 2.45 fm, respectively while ρ_0 can be determined from the normalization condition.

$$4\pi \int \rho(r) r^2 dr = \text{Mass Number}. \quad (4)$$

The DF potential consists mainly of two parts.

The direct part is

$$v_D(r) = \left[11062 \frac{e^{-4r}}{4r} - 2538 \frac{e^{-2.5r}}{2.5r} \right] \text{MeV}, \quad (5)$$

and the knock-on exchange part in the infinite-range exchange is

$$v_{Ex}(r) = \left[-1524 \frac{e^{-4r}}{4r} - 518.8 \frac{e^{-2.5r}}{2.5r} - 7.847 \frac{e^{-0.7072r}}{0.7072r} \right]. \quad (6)$$

In the present work, the modified version of CDM3Y6 interaction based on the inclusion of the rearrangement term (RT) is used, and is denoted by (CDM3Y6-RT). This effective interaction (CDM3Y6-RT) uses another density dependent version (CDM3Y6) of the M3Y effective NN interaction based on the G-matrix elements of Paris potential for the direct and exchange terms Eqs. (5) and (6). The full CDM3Y6 interaction form is defined as [24],

$$v_{D(Ex)}(\rho, r) = g(E) F(\rho) v_{D(Ex)}(r), \quad (7)$$

where, the density dependent function F is written as [25]

$$F(\rho) = 0.2658 [1 + 3.8033 \exp(-1.41\rho - 4.0\rho)], \quad (8)$$

and $g(E)$ is the additional energy dependent factor written as [24],

$$g(E) = [1 - 0.003(E/A)]. \quad (9)$$

For the modified (CDM3Y6-RT) interaction with the inclusion of RT term, the term $\Delta F(\rho)$ is added in the folding model calculation, where $\Delta F(\rho)$ can be written as [25],

$$\Delta F(\rho) = 1.5 [\exp(-0.833\rho) - 1]. \quad (10)$$

2.1. Analysis of ${}^9\text{Be} + {}^{208}\text{Pb}$

The ${}^9\text{Be} + {}^{208}\text{Pb}$ data in the energy range of 37.0 – 75.0 MeV is reanalyzed from the phenomenological point of view using OM. Then, this nuclear system is analyzed semi-microscopically using double folding optical model (DFOM). In this model, the real part of the potential was constructed by folding the density distributions of ${}^9\text{Be}$ and ${}^{208}\text{Pb}$ with nucleon-nucleon interaction potential of the M3Y form with and without taking into consideration the effect of rearrangement term, namely, DFOM and DFOM-RT, in addition to a phenomenological WS imaginary potential of parameters fixed to those obtained from OM analysis. Finally, the ${}^9\text{Be} + {}^{208}\text{Pb}$ data in the aforementioned energy range is subjected to a fully microscopic analysis based on cluster folding model (CFM) for both real and imaginary parts. The cluster folding calculations were constructed based on the ${}^7\text{Li} + d$ cluster structure of ${}^9\text{Be}$. The required ingredients to prepare the cluster folding potential for both the real and imaginary parts are: the ${}^7\text{Li} + {}^{208}\text{Pb}$ and $d + {}^{208}\text{Pb}$ potentials at appropriate energies as well as the ${}^7\text{Li} + d$ binding potential. As the experimental data for ${}^9\text{Be} + {}^{208}\text{Pb}$ elastic scattering angular distribution at $E_{\text{lab}}({}^9\text{Be}) = 75.0$ MeV is the highest energy under consideration, the required potentials are:

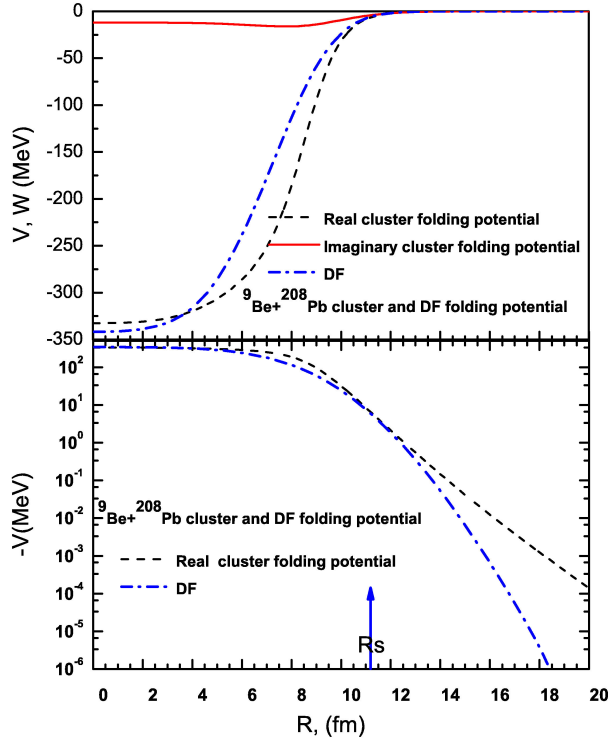


FIGURE 1. Real and imaginary parts of ${}^9\text{Be}+{}^{208}\text{Pb}$ cluster folding potential constructed on the ${}^7\text{Li} + d$ cluster structure for ${}^9\text{Be}$.

${}^7\text{Li} + {}^{208}\text{Pb}$ potential at $E_{\text{lab}}({}^7\text{Li}) = 7/9 \times 75 = 58.3$ MeV and the $d + {}^{208}\text{Pb}$ potential at $E_{\text{lab}}(d) = 2/9 \times 75 = 16.7$ MeV. Fortunately, there are available experimental measurements for ${}^7\text{Li} + {}^{208}\text{Pb}$ angular distribution at $E_{\text{lab}} = 63$ MeV [26] which is close to the required 58.3 MeV, and for $d + {}^{208}\text{Pb}$ at $E_{\text{lab}} = 17$ MeV [27] which is close to the required 16.7 MeV. The real and imaginary cluster folding parts of the ${}^9\text{Be} + {}^{208}\text{Pb}$ potential can be defined on the basis of ${}^7\text{Li} + {}^{208}\text{Pb}$ and $d + {}^{208}\text{Pb}$ potentials as follows:

$$V^{CF}(R) = \int \left(V_{7\text{Li}-208\text{Pb}} \left[\mathbf{R} - \frac{2}{9}\mathbf{r} \right] + V_{d-208\text{Pb}} \left[\mathbf{R} + \frac{7}{9}\mathbf{r} \right] \right) |\chi_{7\text{Li}-d}(\mathbf{r})|^2 d\mathbf{r}, \quad (11)$$

$$W^{CF}(R) = \int \left(W_{7\text{Li}-208\text{Pb}} \left[\mathbf{R} - \frac{2}{9}\mathbf{r} \right] + W_{d-208\text{Pb}} \left[\mathbf{R} + \frac{7}{9}\mathbf{r} \right] \right) |\chi_{7\text{Li}-d}(\mathbf{r})|^2 d\mathbf{r}, \quad (12)$$

where $V_{7\text{Li}-208\text{Pb}}$, $W_{7\text{Li}-208\text{Pb}}$, $V_{d-208\text{Pb}}$, and $W_{d-208\text{Pb}}$ are the optimal real and imaginary potentials for the ${}^7\text{Li} + {}^{208}\text{Pb}$ and $d + {}^{208}\text{Pb}$ channels, respectively, which were taken the same as those in Ref. [26,27]. The term $\chi_{7\text{Li}-d}(\mathbf{r})$ is the inter-cluster wave function for the relative motion of ${}^7\text{Li}$ and d in the ground state of ${}^9\text{Be}$ and \mathbf{r} is the relative coordinate between the centers of mass of ${}^7\text{Li}$ and d . The ${}^7\text{Li}-d$ bound state form factor represents a $2S_1$ state in a real Woods-Saxon

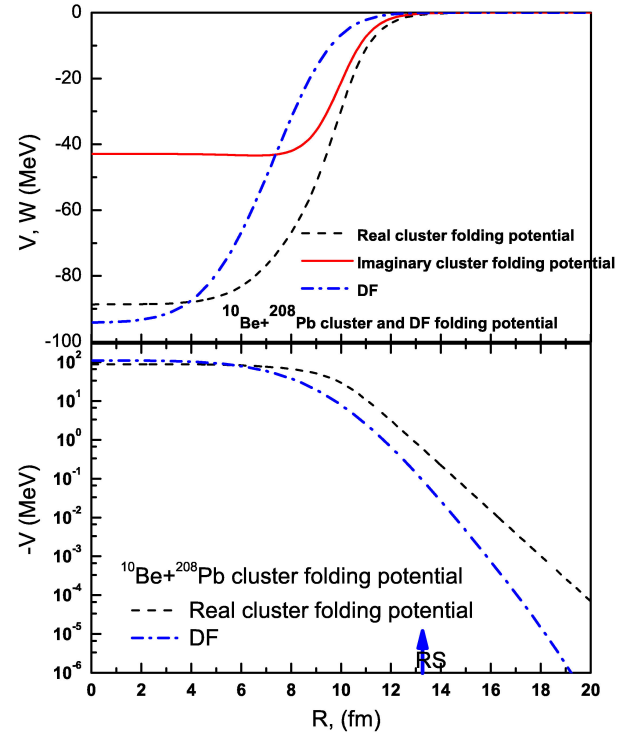


FIGURE 2. Real and imaginary parts of ${}^{10}\text{Be}+{}^{208}\text{Pb}$ cluster folding potential constructed on the ${}^9\text{Be} + n$ cluster structure for ${}^{10}\text{Be}$.

potential with $V_0 = 79.0$ MeV, $R = 1.15$ fm, $a = 0.7$ fm. The generated cluster folding potential for ${}^9\text{Be}+{}^{208}\text{Pb}$ is shown in Fig. 1.

2.2. Analysis of ${}^{10}\text{Be}+{}^{208}\text{Pb}$

The available experimental angular distributions for ${}^{10}\text{Be}+{}^{208}\text{Pb}$ elastic scattering at energies $E_{\text{lab}} = 38.4, 39, 39.9, 42.6,$ and 43.9 MeV [10] are reanalyzed from the phenomenological and the semi-microscopic point of view. Firstly, the OM analysis was performed utilizing OM potential consisting from real and imaginary volume parts, each having the conventional WS form in addition to a Coulomb part “see Eq. (1)”. The analysis was performed using fixed radii parameters. Then, on the basis of the ${}^9\text{Be} + n$ cluster structure of ${}^{10}\text{Be}$, the considered data are reanalyzed using cluster folding model. The required ingredients to perform cluster folding calculations for ${}^{10}\text{Be} + {}^{208}\text{Pb}$ by considering the proposed ${}^9\text{Be} + n$ cluster structure of ${}^{10}\text{Be}$ are: the ${}^9\text{Be} + {}^{208}\text{Pb}$ potential at $E_{\text{lab}}({}^9\text{Be}) = 9/10 \times E_{\text{lab}}({}^{10}\text{Be})$, $n + {}^{208}\text{Pb}$ potential at $E_{\text{lab}}(n) = 1/10 \times E_{\text{lab}}({}^{10}\text{Be})$ and $n + {}^9\text{Be}$ binding potential. For ${}^{10}\text{Be} + {}^{208}\text{Pb}$ elastic scattering angular distributions in the energy range 38.4 – 43.9 MeV, the highest energy under consideration is $E_{\text{lab}}({}^{10}\text{Be}) = 43.9$ MeV. Fortunately there are available experimental measurements for ${}^9\text{Be} + {}^{208}\text{Pb}$ angular distribution at $E_{\text{lab}}({}^9\text{Be}) = 39.6$ MeV [11]. The real and imaginary cluster folding parts of the ${}^{10}\text{Be} + {}^{208}\text{Pb}$ potential can be defined on the basis of ${}^9\text{Be} + {}^{208}\text{Pb}$ and $n + {}^{208}\text{Pb}$ potentials as follows:

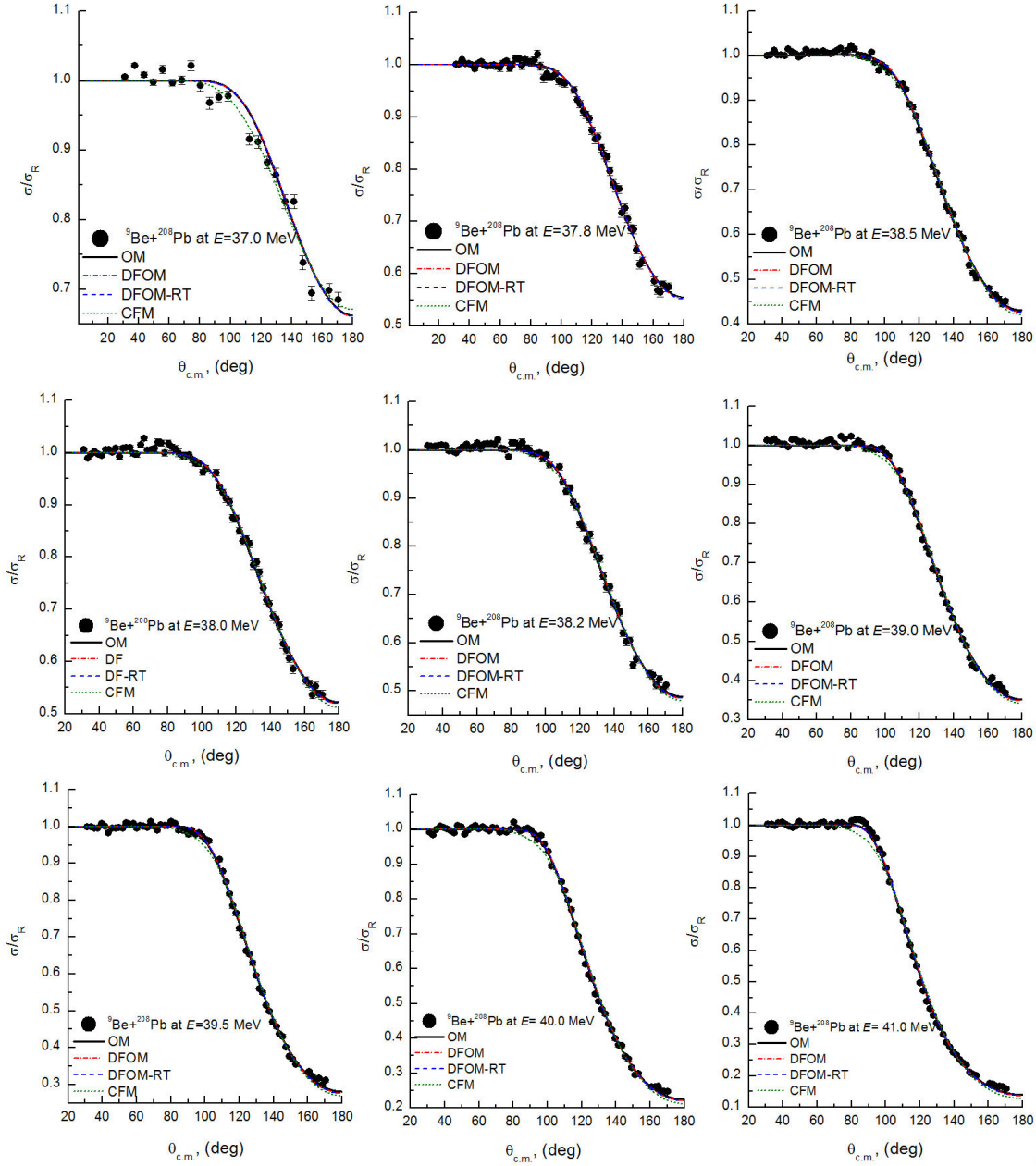


FIGURE 3. Comparison between ${}^9\text{Be}+{}^{208}\text{Pb}$ elastic scattering angular distributions at $E_{lab} = 37.0, 37.8, 38.0, 38.2, 38.5, 39.0, 39.5, 40.0,$ and 41.0 MeV and theoretical calculations using OM (solid lines), DFOM (dash dot lines), DFOM-RT (dash lines), and CFM (short dash lines).

$$V^{CF}(R) = \int \left(V_{9\text{Be}-208\text{Pb}} \left[\mathbf{R} - \frac{1}{10} \mathbf{r} \right] + V_{n-208\text{Pb}} \left[\mathbf{R} + \frac{9}{10} \mathbf{r} \right] \right) |\chi_{9\text{Be}-n}(\mathbf{r})|^2 d\mathbf{r}, \quad (13)$$

$$W^{CF}(R) = \int \left(W_{9\text{Be}-208\text{Pb}} \left[\mathbf{R} - \frac{1}{10} \mathbf{r} \right] + W_{n-208\text{Pb}} \left[\mathbf{R} + \frac{9}{10} \mathbf{r} \right] \right) |\chi_{9\text{Be}-n}(\mathbf{r})|^2 d\mathbf{r}, \quad (14)$$

where $V_{9\text{Be}-208\text{Pb}}$, $W_{9\text{Be}-208\text{Pb}}$, $V_{n-208\text{Pb}}$, and $W_{n-208\text{Pb}}$ are the optimal real and imaginary potentials for the ${}^9\text{Be} + {}^{208}\text{Pb}$ and $n + {}^{208}\text{Pb}$ channels, respectively, which were taken the same as those in Ref. [11,28]. The term $\chi_{9\text{Be}-n}(\mathbf{r})$ is the inter-cluster wave function for the relative motion of ${}^9\text{Be}$ and n in the ground state of ${}^{10}\text{Be}$, and \mathbf{r} is the relative coordinate between the centers of mass of ${}^9\text{Be}$ and n . The bound state potential which bind the core (${}^9\text{Be}$) with the valence particle (n) orbiting this core was taken of phenomenological Woods-Saxon potential of diffuseness $a_b=0.7$ fm and radius $r_b=1.15$ fm. The potential depth V_b was found by fitting to the cluster binding energy (B.E=6.812 MeV).

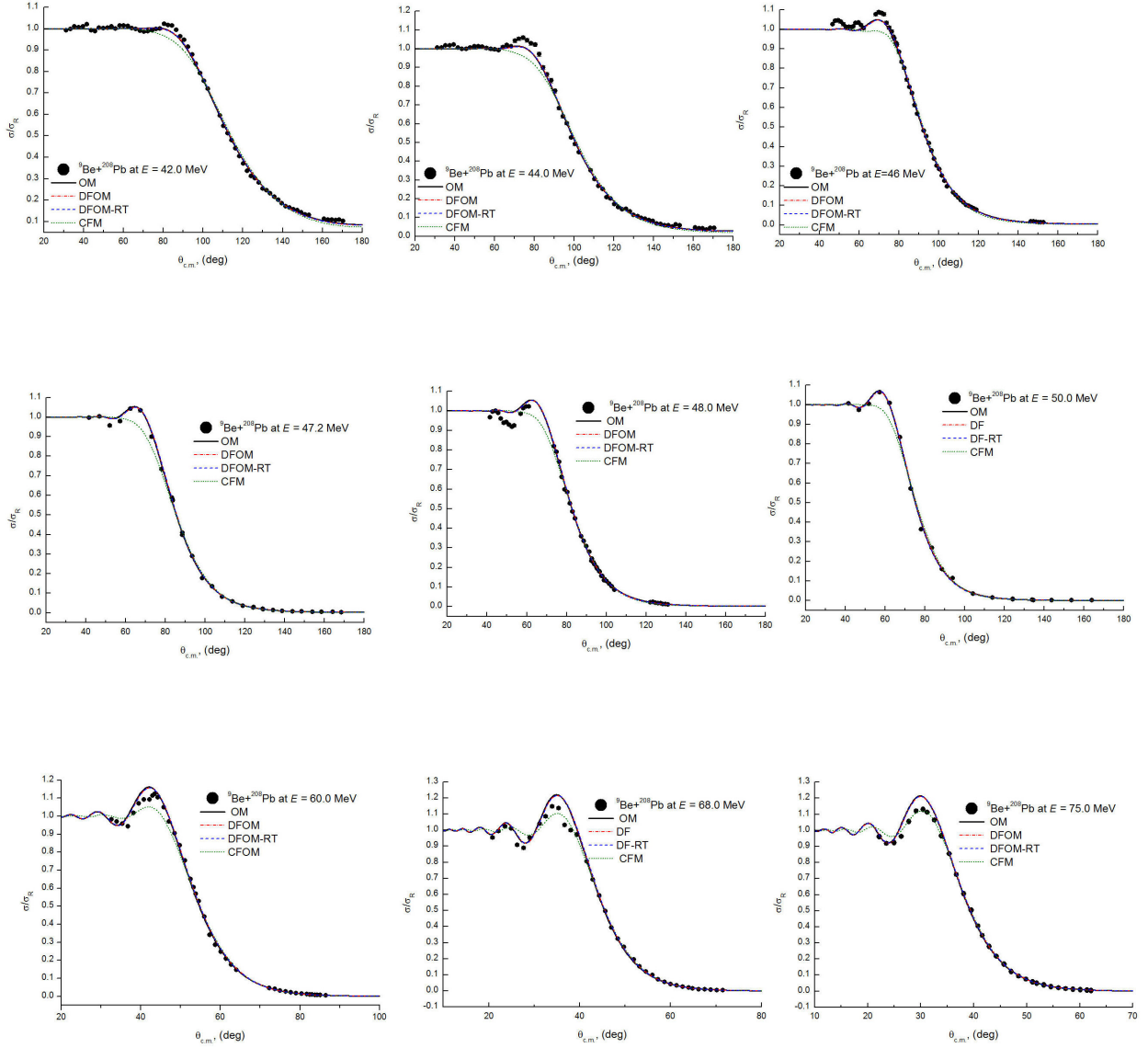


FIGURE 4. Same as Fig. 3 but at $E_{lab} = 42.0, 44.0, 46.0, 47.2, 48.0, 50.0, 60.0, 68.0,$ and 75.0 MeV.

The generated cluster folding potential for ${}^{10}\text{Be}+{}^{208}\text{Pb}$ is shown in Fig. 2. To validate our analysis, we plotted expression (11) for ${}^9\text{Be}+{}^{208}\text{Pb}$ at 75 MeV and expression (13) for ${}^{10}\text{Be}+{}^{208}\text{Pb}$ at 48.3 MeV, respectively, against the DF potential with finite-range exchange contribution for the densities under consideration, as shown in Figs. 1 and 2. At ($R=0$), $(V^{\text{Cluster}}(0)/V^{\text{DF}}(0))\approx 0.95$, this means that the scattering is sensitive to the real potential for both the considered systems. These two figures show that, the DF potential is about 5% deeper than the cluster potential at ($R=0$), while they are similar for radial distances R ranging from 0.5 fm to 7 fm.

A strong absorption radius R_S (closest approach) through the surface radial region can be defined as the distance between colliding particles in terms of the transmission coefficient $T_{1/2}$, which is a function of the partial wave and mo-

mentum $L_{1/2}$, as well as the Sommerfield parameter η and the projectile wave number k [13]. We can see that the different DF and cluster potentials agree with each other near the strong absorption radius R_S where $R_S = 11.1$ fm for the ${}^9,{}^{10}\text{Be}+{}^{208}\text{Pb}$ reaction.

3. Results and discussion

3.1. ${}^9\text{Be}+{}^{208}\text{Pb}$ nuclear system

The comparison between the experimental ${}^9\text{Be}+{}^{208}\text{Pb}$ elastic scattering angular distributions in the energy range

TABLE I. Optimal potential parameters achieved from our best fit to ${}^9\text{Be} + {}^{208}\text{Pb}$ elastic scattering data in energy range $E_{lab} = 37.0 - 75.0$ MeV using OM, DFOM, DFOM-RT, and CFM potentials.

E	Model	V	r_V	a_V	N_r	W	r_W	a_W	N_{RCF}	N_{ICF}	χ^2/N	σ_R	
37	OM	29.44	1.24	0.63		58.0	1.24	0.63			7.5	107.4	
	DFOM				0.588				70.6	1.24	0.63	7.6	107.4
	DFOM- RT				0.61				70.6	1.24	0.63	7.6	107.4
	CFM											0.456	0.483
37.8	OM	30.9	1.24	0.63		54.3	1.24	0.63			2.2	146.5	
	DFOM				0.604				54.3	1.24	0.63	2.1	146.5
	DFOM- RT				0.627				54.3	1.24	0.63	2.1	146.5
	CFM											0.734	0.390
38	OM	36.1	1.24	0.63		50.0	1.24	0.63			3.5	152.9	
	DFOM				0.697				50.0	1.24	0.63	3.6	152.9
	DFOM- RT				0.724				50.0	1.24	0.63	3.6	152.8
	CFM											0.778	0.366
38.2	OM	40.2	1.24	0.63		46.4	1.24	0.63			3.9	160.6	
	DFOM				0.768				46.4	1.24	0.63	4.1	160.5
	DFOM- RT				0.798				46.4	1.24	0.63	4.1	160.5
	CFM											0.785	0.356
38.5	OM	42.6	1.24	0.63		45.7	1.24	0.63			3.8	182.3	
	DFOM				0.81				45.7	1.24	0.63	3.9	182.2
	DFOM- RT				0.84				45.7	1.24	0.63	3.9	182.1
	CFM											0.783	0.366
39	OM	44.73	1.24	0.63		41.73	1.24	0.63			7.4	212.5	
	DFOM				0.84				41.73	1.24	0.63	8.0	212.3
	DFOM- RT				0.872				41.73	1.24	0.63	8.0	212.2
	CFM											0.766	0.358
39.5	OM	43.07	1.24	0.63		42.86	1.24	0.63			4.6	256.7	
	DFOM				0.804				42.86	1.24	0.63	5.04	256.4
	DFOM- RT				0.836				42.86	1.24	0.63	5.1	256.2
	CFM											0.710	0.387
40	OM	39.89	1.24	0.63		45.7	1.24	0.63			6.4	307.2	
	DFOM				0.741				45.7	1.24	0.63	7.0	306.7
	DFOM- RT				0.772				45.7	1.24	0.63	7.0	306.6
	CFM											0.640	0.425
41	OM	36.02	1.24	0.63		47.07	1.24	0.63			7.04	401.9	
	DFOM				0.663				47.07	1.24	0.63	8.4	401.1
	DFOM- RT				0.693				47.07	1.24	0.63	8.4	401.0
	CFM											0.538	0.469
42	OM	32.53	1.24	0.63		48.37	1.24	0.63			14.35	498.6	
	DFOM				0.596				48.37	1.24	0.63	15.9	497.9
	DFOM- RT				0.624				48.37	1.24	0.63	15.9	497.7
	CFM											0.447	0.512
44	OM	30.97	1.24	0.63		47.41	1.24	0.63			6.2	684.8	
	DFOM				0.563				47.41	1.24	0.63	6.9	683.8
	DFOM- RT				0.592				47.41	1.24	0.63	6.9	683.7
	CFM											0.358	0.562
46	OM	36.39	1.24	0.63		33.15	1.24	0.63			11.4	810.4	
	DFOM				0.662				33.15	1.24	0.63	13.9	809.9
	DFOM- RT				0.696				33.15	1.24	0.63	14.2	809.2
	CFM											0.459	0.44

E	Model	V	r_V	a_V	N_r	W	r_W	a_W	N_{RCF}	N_{ICF}	χ^2/N	σ_R			
47.2	OM	38.16	1.24	0.63		41.17	1.24	0.63			10.2	957.1			
	DFOM				0.688				41.17	1.24			0.63	12.3	955.4
	DFOM- RT				0.723				41.17	1.24			0.63	12.5	954.7
	CFM													0.337	0.655
48	OM	36.09	1.24	0.63		42.11	1.24	0.63			19.2	1020			
	DFOM				0.661				42.11	1.24			0.63	18.7	1020
	DFOM- RT				0.696				42.11	1.24			0.63	18.8	1020
	CFM													0.348	0.628
50	OM	40.38	1.24	0.63		49.13	1.24	0.63			27.4	1217			
	DFOM				0.729				52.09	1.24			0.63	28.5	1215
	DFOM- RT				0.766				52.2	1.24			0.63	28.7	1220
	CFM													0.327	0.716
60	OM	46.5	1.24	0.63		38.27	1.24	0.63			14.1	1775			
	DFOM				0.846				38.27	1.24			0.63	16.1	1774
	DFOM- RT				0.890				38.27	1.24			0.63	16.8	1772
	CFM													0.418	0.703
68	OM	45.14	1.24	0.63		27.97	1.24	0.63			33.8	2039			
	DFOM				0.822				27.97	1.24			0.63	26.5	2037
	DFOM- RT				0.864				27.97	1.24			0.63	26.2	2034
	CFM													0.442	0.618
75	OM	45.49	1.24	0.63		33.67	1.24	0.63			20.7	2314			
	DFOM				0.844				33.67	1.24			0.63	17.3	2314
	DFOM- RT				0.889				33.67	1.24			0.63	16.9	2312
	CFM													0.453	0.645

37.0 – 75.0 MeV and the OM, DFOM, DFOM-RT, and CFM calculations performed using FRESKO code [29] are shown in Figs. 3 and 4 using the potential parameters listed in Table I. In OM calculations, the analysis was performed using two adjustable parameters real and imaginary potential depths V_0 and W_0 , while the real and imaginary radius and diffuseness parameters were kept fixed at 1.24 and 0.63 fm respectively. The potential parameters considered in Ref. [11] for both the real and imaginary parts of potential were taken as starting parameters. It is clearly shown in Figs. 3 and 4, that the agreement between experimental data and OM calculations is fairly good even in the angular range where the Coulomb rainbow phenomenon is well presented. Although similar OM calculations were performed for ${}^9\text{Be}+{}^{208}\text{Pb}$ system in the energy range 37.0–50.0 [11], it was necessary also in the current study to start our analysis from the pure phenomenological point of view in order to extract the optimal OM parameters for ${}^9\text{Be}+{}^{208}\text{Pb}$ system in the whole considered energy range. The optimal extracted imaginary potential parameters were implemented in the semi-microscopic analysis. In DFOM calculations, two approaches were used: DFOM and DFOM-RT in order to study the effect of introducing the rearrangement term. As expected, in order to describe ${}^9\text{Be}+{}^{208}\text{Pb}$ data, the strength of the real part should be reduced by $\sim 25 - 28\%$. The extracted average renormalization factor for the real part of the potential is 0.72 ± 0.095 and 0.75 ± 0.099 from DFOM and DFOM-RT calculations, respectively. The experimental data is reasonably reproduced

by DFOM with nearly the same good fitting as shown in Figs. 3 and 4, whereas the DFOM-RT clearly provides a poorer description, particularly in the Coulomb rainbow region.

Finally, the ${}^9\text{Be}+{}^{208}\text{Pb}$ elastic scattering angular distributions in the energy range 37.0 – 75.0 MeV are analyzed within the framework of CFM. The CFM analysis was performed using two free parameters N_{RCF} and N_{ICF} , namely renormalization factor for the real and imaginary cluster folding potential, respectively. These two parameters are allowed to be freely changed in the range 0.2 – 1.3 till reach the best agreement the experimental data and the theoretical calculations by minimizing the χ^2/N value. As shown in Figs. 3 and 4, the comparison between the experimental angular distributions for ${}^9\text{Be}+{}^{208}\text{Pb}$ nuclear system and theoretical calculations within the frame work of CFM is fairly good except in the angular range where Fresnel peak is presented especially at energies less than 60 MeV. At higher energies greater than 60 MeV, the CFM calculations reproduce well the Fresnel peak. In order to reproduce the experimental data using CFM, the strength of the real cluster folding parts should be reduced by $\sim 0.45\%$. The extracted average N_{RCF} and N_{ICF} values are 0.55 ± 0.18 and 0.45 ± 0.13 , respectively. These results emphasize the weak nature of ${}^9\text{Be}$.

As shown in Fig. 5, the Coulomb rainbow phenomenon (Fresnel peak) which resulted from the interference between Coulomb and nuclear potential is well presented at energies above 40 MeV. It is obvious that with increasing the projec-

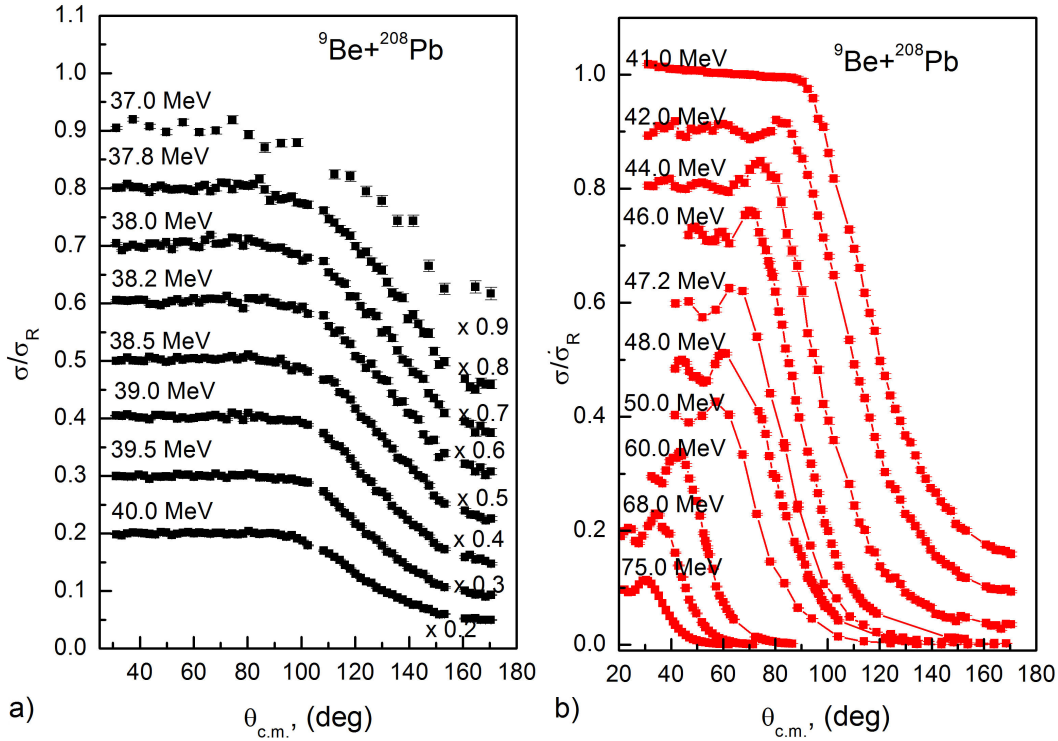


FIGURE 5. Angular distributions for ${}^9\text{Be}+{}^{208}\text{Pb}$ elastic scattering in the energy range 37.0 – 75.0 MeV. Data are displaced by 0.1 for the sake of clarity. Left panel for energies 37.0 – 40. MeV where Coulomb rainbow phenomenon is not observed. Right panel for energies 41.0 – 75.0 MeV where Coulomb rainbow phenomenon is observed.

TABLE II. Optimal potential parameters achieved from our best fit to the measured data of ${}^{10}\text{Be} + {}^{208}\text{Pb}$ elastic scattering at $E_{lab}=38.4\text{--}43.9$ MeV using OM with fixed $r_v=1.355$ and $r_w=1.338$ fm as well as CFM.

E (MeV)		V	a_V	W	a_W	N_{RCF}	N_{ICF}	χ^2/N	σ_R
38.4	OM	25.0	0.25	33.79	0.25			0.37	11.67
	CFM					0.2	0.205	0.7	45.15
39.0	OM	25.0	0.25	29.96	0.264			0.19	21.57
	CFM					0.2	0.2	0.5	57.9
39.9	OM	25.0	0.49	28.6	0.413			0.19	211.7
	CFM					0.267	1.01	0.55	310.9
42.6	OM	25.0	0.452	25.0	0.32			1.06	379.7
	CFM					0.311	0.997	1.98	577.4
43.9	OM	25.0	0.405	25.0	0.543			1.12	700.1
	CFM					0.315	0.981	1.12	700.7

TABLE III. Optimal potential parameters achieved from our best fit to the measured data of ${}^{10}\text{Be} + {}^{208}\text{Pb}$ elastic scattering at $E_{lab}=38.4\text{--}43.9$ MeV using CFM of non-renormalized $N_{RCF}=1$ and $N_{ICF}=1$ plus DPP, the approach CFM+DPP.

E (MeV)	V_0	W_0	χ^2/N	σ_R
38.4	-30.19	-11.05	0.21	24.15
39.0	-13.83	-11.89	0.18	13.50
39.9	-8.15	-7.35	0.22	220.1
42.6	-9.13	-10.81	0.88	304.7
43.9	-12.23	-2.83	1.18	661.2

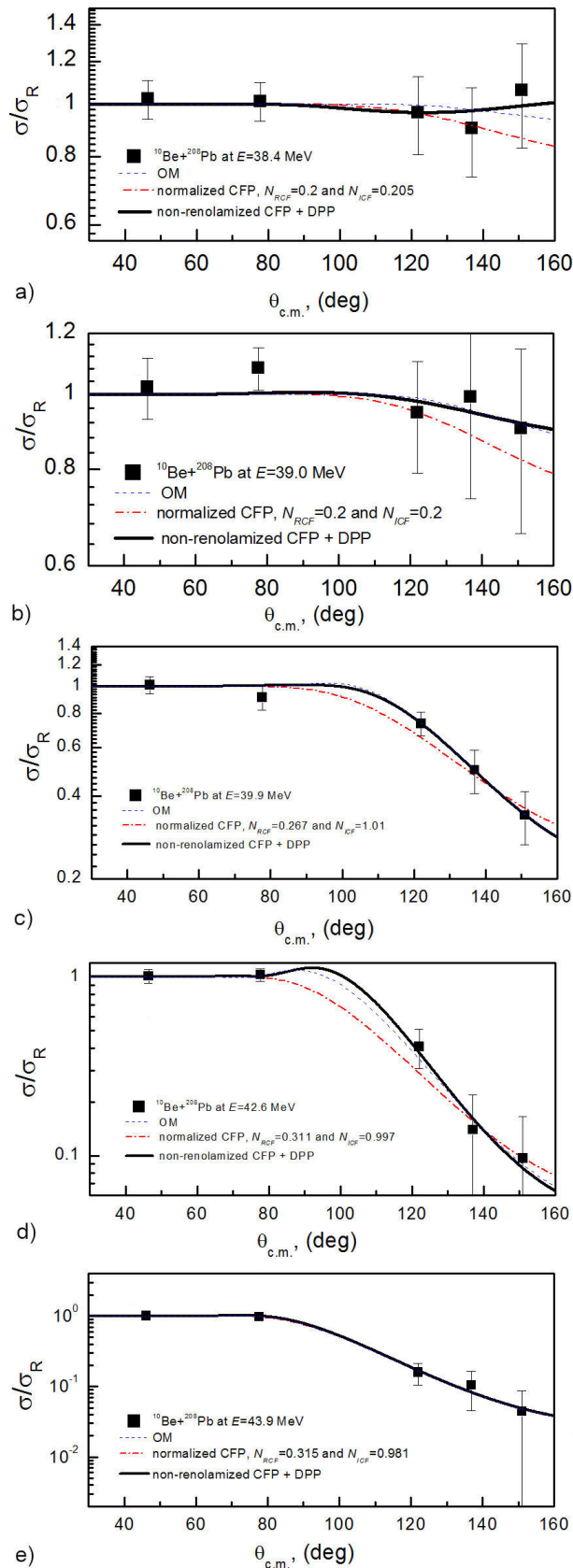


FIGURE 6. Comparison of elastic scattering angular distributions of $^{10}\text{Be}+^{208}\text{Pb}$ at $E_{lab} = 38.4, 39.0, 39.9, 42.6,$ and 43.9 MeV with theoretical calculations using OM, CFM, and CFM+DPP.

tile energy, the position of Fresnel peak is shifted towards smaller angles.

3.2. $^{10}\text{Be}+^{208}\text{Pb}$ nuclear system

The comparison between the experimental angular distributions for $^{10}\text{Be}+^{208}\text{Pb}$ nuclear system and theoretical calculations within the frame work of OM in the energy range 38.4 – 43.9 MeV is shown in Fig. 6. The OM calculations were performed by fixing radii parameters r_V and r_W to the values 1.355 and 1.338 fm, respectively and by allowing the other four parameters (real and imaginary potential depth and diffuseness) to be changed freely till reach the best agreement between the experimental data and the theoretical calculations by minimizing the χ^2/N value as shown in Table II. The CFM analysis was performed using two free parameters N_{RCF} and N_{ICF} . These two parameters are allowed to be freely changed in the range 0.2 – 1.2 till reach the best agreement between the experimental data and the theoretical calculations as shown in Fig. 6 using potential parameters listed in Table II. In order to reproduce the data within the frame work of CFM, the strength of real part of potential should be reduced by about 74 % which reflect the weak nature of ^{10}Be .

Finally, $^{10}\text{Be}+^{208}\text{Pb}$ elastic scattering angular distributions in the aforementioned energy range are reanalyzed using the previously created cluster folding potential but without renormalizing the real and imaginary cluster potential parts (N_{RCF} and $N_{ICF} = 1$) plus a dynamical polarization potential DPP in the form of Woods-Saxon and has a repulsive surface nature, namely CFM+DPP, to compensate the observed reduction in the strength of real and imaginary CF parts of potential. The dynamical polarization potential for both the real and imaginary parts has been fixed ($r_{V\text{pol}} = r_{W\text{pol}} = 1.24$ fm) and ($a_{V\text{pol}} = a_{W\text{pol}} = 0.63$ fm). Two parameters are allowed to be changed freely until they achieved the best agreement between data and calculations: real and imaginary dynamical polarization potential

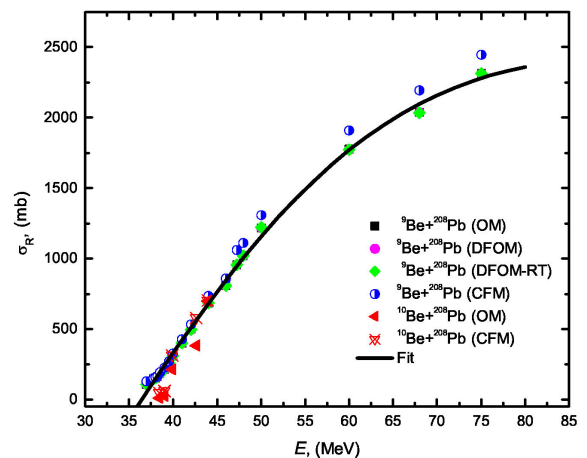


FIGURE 7. Energy dependence on reaction cross sections for $^{9,10}\text{Be}+^{208}\text{Pb}$ systems based on the different considered approaches (OM, DFOM, DFOM-RT and CFM).

depths, V_{pol} and W_{pol} . The comparison between the experimental angular distributions for the $^{10}\text{Be}+^{208}\text{Pb}$ nuclear system and the CFM+DPP calculations is shown in Fig. 6 using the potential parameters listed in Table III.

As the total reaction cross section σ_R is a useful quantity to test the validity of calculations, the energy dependence on σ_R is studied for the two systems - $^{9,10}\text{Be}+^{208}\text{Pb}$ - under consideration. As shown in Fig. 7, it is found that the extracted σ_R values for $^{9,10}\text{Be}+^{208}\text{Pb}$ systems utilizing the different considered approaches (OM, DFOM, DFOM-RT and CFM) are close to each other and can be expressed by quadratic polynomial function $\sigma_R(E) = -5370 + 196 E - 1.431 E^2$.

4. Summary

The current study's main goal is to conduct a further analysis of the interaction mechanism and peculiarities resulting from the scattering of Beryllium isotopes $^{9,10}\text{Be}$ from the heavy target ^{208}Pb . In accordance with this aim, the following nuclear systems: $^9\text{Be}+^{208}\text{Pb}$ in the energy range 37.0 – 75.0 MeV and $^{10}\text{Be}+^{208}\text{Pb}$ in the energy range 38.4 – 127 MeV are investigated using different potentials. OM analysis as expected could fairly reproduce the considered experimental data. Analysis performed within the frame work of DF

with and without taking into consideration the effect of rearrangement term as well as CFM calculations, reflected the weak nature of ^9Be and ^{10}Be . The same trend was also observed in DF and CF analysis for the scattering of ^6Li from various target nuclei [30-33]. For $^9\text{Be}+^{208}\text{Pb}$ nuclear system, the strength of the real double folded part should be reduced by $\sim 25 - 28 \%$ in order to reproduce the data. A similar trend was also observed in CFM analysis; the strength of the real cluster folding part should be reduced by $\sim 0.45 \%$. For the $^{10}\text{Be}+^{208}\text{Pb}$ nuclear system, CFM analysis was performed using two free parameters N_{RCF} and N_{ICF} . The strength of real cluster folding part of potential should be reduced by about 74 % to obtain a good fit with the data. The performed analysis again showed that, the reduction in the strength of DF and CF potentials for nuclear systems induced by the weakly $^{9,10}\text{Be}$ isotopes could reflect the weak binding nature of these isotopes.

Acknowledgement

A.A. Ibraheem extends his appreciation to the Deanship of Scientific Research at King Khalid University for funding this work through research groups program under grant number R.G.P.1/1/42

1. L. F. Canto, P. R. S. Gomes, R. Donangelo, and M. S. Hussein, *Fusion and breakup of weakly bound nuclei*, Phys. Rep. **424** 1 (2006), <https://doi.org/10.1016/j.physrep.2005.10.006>.
2. N. Keeley, R. Raabe, N. Alamanos, and J. L. Sida, *Fusion and direct reactions of halo nuclei at energies around the Coulomb barrier*, Prog. Part. Nucl. Phys. **59**, 579 (2007), <https://doi.org/10.1016/j.ppnp.2007.02.002>.
3. N. Keeley, N. Alamanos, K. W. Kemper, and K. Rusek, *Elastic scattering and reactions of light exotic beams*, Prog. Part. Nucl. Phys. **63**, 396 (2009), <https://doi.org/10.1016/j.ppnp.2009.05.003>.
4. L. F. Canto, P. R. S. Gomes, R. Donangelo, J. Lubian, and M. S. Hussein, *Recent developments in fusion and direct reactions with weakly bound nuclei*, Phys. Rep. **596**, 1 (2015) <https://doi.org/10.1016/j.physrep.2015.08.001>.
5. J. J. Kolata, V. Guimarães, and E. F. Aguilera, *Elastic scattering, fusion, and breakup of light exotic nuclei*, Eur. Phys. J. A **52** (2016) 123, <https://doi.org/10.1140/epja/i2016-16123-1>.
6. G. Montagnoli and A. M. Stefanini, *Recent experimental results in sub- and near-barrier heavy-ion fusion reactions*, Eur. Phys. J. A **53** 169 (2017), <https://doi.org/10.1140/epja/i2017-12350-2>.
7. A. Bonaccorso, *Direct reaction theories for exotic nuclei: An introduction via semi-classical methods*, Prog. Part. Nucl. Phys. **101**, 1 (2018), <https://doi.org/10.1016/j.ppnp.2018.01.005>.
8. V. Jha, V. V. Parkar, and S. Kailas, *Incomplete fusion reactions using strongly and weakly bound projectiles*, Phys. Rep. **845**, 1 (2020), <https://doi.org/10.1016/j.physrep.2019.12.003>.
9. R. J. Woolliscroft *et al.*, *Elastic scattering and fusion of $^9\text{Be} + ^{208}\text{Pb}$: Density function dependence of the double folding renormalization*, Phys. Rev. C **69** (2004) 044612 <https://link.aps.org/doi/10.1103/PhysRevC.69.044612>.
10. J.J. Kolata, *et al.*, *Elastic scattering of ^{10}Be on ^{208}Pb near the Coulomb barrier*, Physical Review, **C69** (2004) 047601, <https://link.aps.org/doi/10.1103/PhysRevC.69.047601>.
11. Ning Yu *et al.*, *Unusual potential behavior for the weakly bound nucleus ^8Be in elastic scattering from ^{208}Pb and ^{209}Bi near the threshold*, Journal of Physics: Nuclear Physics, **G37** (2010) 075108, <https://doi.org/10.1088/0954-3899/37/7/075108>.
12. F.F. Duan *et al.*, *Scattering of the halo nucleus ^{11}Be from a lead target at 3.5 times the Coulomb barrier energy*, Physics Letters **B811**(2020)135942, <https://doi.org/10.1016/j.physletb.2020.135942>.
13. G. R. Satchler and W. G. Love, *Folding model potentials from realistic interactions for heavy-ion scattering*, phys. Rep. **55** (1979) 183, [https://doi.org/10.1016/0370-1573\(79\)90081-4](https://doi.org/10.1016/0370-1573(79)90081-4).
14. G. R. Satchler, *The optical potential for ^9Be scattering: Another anomaly*, Phys. Lett. B **83** (1979) 284, [https://doi.org/10.1016/0370-2693\(79\)91108-0](https://doi.org/10.1016/0370-2693(79)91108-0).

15. J.S.Eck, T.R.Ophel, P.D.Clark, D.C.Weisser, Classical and potential descriptions of ${}^9\text{Be}+{}^{28}\text{Si}$ and ${}^9\text{Be}+{}^{40}\text{Ca}$ elastic scattering cross sections at $E_{9\text{Be}}=45$ and 60 MeV, Nuclear Physics **A334**(1980)519, [https://doi.org/10.1016/0375-9474\(80\)90615-6](https://doi.org/10.1016/0375-9474(80)90615-6).
16. V. Hnizdo, J. Szymakowski, K. W. Kemper, and J. D. Fox, Folding-model description of elastic and inelastic scattering of ${}^9\text{Be}$ by ${}^{40,44}\text{Ca}$ and ${}^{39}\text{K}$ at 40 MeV; Phys. Rev **C24**(1981)1495. <https://link.aps.org/doi/10.1103/PhysRevC.24.1495>.
17. Awad A. Ibraheem *et al.*, Elastic and Inelastic Scattering of ${}^9,{}^{10,}{}^{11}\text{Be}$ by ${}^{64}\text{Zn}$ and ${}^{120}\text{Sn}$ Nuclei at Different Energies, Braz. J. Phys. **51** (2021) 753, <https://doi.org/10.1007/s13538-020-00839-7>.
18. Bertsch G F, Borysowicz J, Mcmanus H and Ae W G, Interactions for inelastic scattering derived from realistic potentials, Nucl. Phys. A **284** (1977) 399, [https://doi.org/10.1016/0375-9474\(77\)90392-x](https://doi.org/10.1016/0375-9474(77)90392-x).
19. Anantaraman N, Toki H and Bertsch G F, An effective interaction for inelastic scattering derived from the Paris potential, Nucl. Phys. A **398** (1983) 269, [https://doi.org/10.1016/0375-9474\(83\)90487-6](https://doi.org/10.1016/0375-9474(83)90487-6).
20. M. El-Azab Farid and G. R. Satchler, A density-dependent interaction in the folding model for heavy-ion potentials, Nucl. Phys. A **438** (1985) 525, [https://doi.org/10.1016/0375-9474\(85\)90391-4](https://doi.org/10.1016/0375-9474(85)90391-4).
21. <https://www.phy.anl.gov/theory/research/density/>.
22. R.E. Warner *et al.*, Total reaction and $2n$ -removal cross sections of $20\text{--}80\text{A MeV}$ ${}^4,{}^6,{}^8\text{He}$, ${}^{6-9,}{}^{11}\text{Li}$, and ${}^{10}\text{Be}$ on Si, Phys. Rev. **C54** (1996) 1700, <https://link.aps.org/doi/10.1103/PhysRevC.54.1700>.
23. M. El-Azab Farid and M. A. Hassanain, Density-independent folding analysis of the ${}^6,{}^7\text{Li}$ elastic scattering at intermediate energies, Nucl. Phys. **A678**, 39 (2000), [https://doi.org/10.1016/S0375-9474\(00\)00313-4](https://doi.org/10.1016/S0375-9474(00)00313-4).
24. D. T. Khoa, G. R. Satchler, and W. von Oertzen, Nuclear incompressibility and density dependent NN interactions in the folding model for nucleus-nucleus potentials, Phys. Rev. **C 56** (1997) 954, <https://link.aps.org/doi/10.1103/PhysRevC.56.954>.
25. Dao T. Khoa Nguyen Hoang Phuc, Doan Thi Loan and Bui Minh Loc, Nuclear mean field and double-folding model of the nucleus-nucleus optical potential, Phys. Rev. **C 94** (2016) 034612. <https://link.aps.org/doi/10.1103/PhysRevC.94.034612>.
26. H. Utsunomiya, *et al.*, Continuous distribution of relative kinetic energies in ${}^7\text{Li}$ breakup reactions, Nucl. Phys. A **511** (1990) 379, [https://doi.org/10.1016/0375-9474\(90\)90165-I](https://doi.org/10.1016/0375-9474(90)90165-I).
27. J. D. Childs, w. w. Daehnick and M. J. Spisak, Accurate elastic scattering cross sections for 17-MeV deuterons, Phys. Rev. **C 10** (1974) 217. <https://link.aps.org/doi/10.1103/PhysRevC.10.217>.
28. J.R.M. Annand, R.W. Finlay, P.S. Dietrich, A low-energy optical-model analysis of ${}^{208}\text{Pb}$ and ${}^{209}\text{Bi}$, Nuclear Physics A **443** (1985)249, [https://doi.org/10.1016/0375-9474\(85\)90263-5](https://doi.org/10.1016/0375-9474(85)90263-5).
29. I. J. Thompson, Coupled reaction channels calculations in nuclear physics, Comput. Phys. Rep. **7** (1988) 167, [https://doi.org/10.1016/0167-7977\(88\)90005-6](https://doi.org/10.1016/0167-7977(88)90005-6).
30. Sh. Hamada and Awad A. Ibraheem, Peculiarities of ${}^6\text{Li}+{}^{12}\text{C}$ elastic scattering, Int.J. Mod. Phys. **E28** (2019) 1950108, <https://doi.org/10.1142/S0218301319501088>.
31. Sh. Hamada, B. Alshahrani, AbdElrahman Elgamala, N. Darwish, I. Bondouk and Awad A. Ibraheem, Analysis of ${}^6\text{Li}+{}^{16}\text{O}$ elastic scattering using different potentials, Revista Mexicana de Fisica **66** (2020) 322, <https://doi.org/10.31349/RevMexFis.66.322>.
32. Sh. Hamada and Awad A. Ibraheem, Cluster folding optical potential analysis for ${}^6\text{Li}+{}^{28}\text{Si}$ elastic scattering, Revista Mexicana de Fisica **67** (2021) 276, <https://doi.org/10.31349/RevMexFis.67.276>.
33. Sh. Hamada, Norah A. M. Alsaif and Awad A. Ibraheem, Detailed analysis for ${}^6\text{Li}+{}^{40}\text{Ca}$ elastic scattering using different potentials, Phys. Scr. **96** (2021) 055306, <https://doi.org/10.1088/1402-4896/abeba6>.